Assimilation of SBAS-InSAR Based Vertical Deformation Into Land Surface Model to Improve the Estimation of Terrestrial Water Storage

Kun Chen , Guoxiang Liu , Wei Xiang, Tao Sun, Kun Qian, Jiaxin Cai, Saied Pirasteh , and Xiao Chen

Abstract—The gravity recovery and climate experiment (GRACE) provides an unprecedented opportunity to detect the spatial and temporal variation of the terrestrial water storage (TWS) for regional to continental scales. However, the GRACE system's coarse temporal resolution (∼monthly) and data discontinuity missing perplexed the TWS research during the operation. In this article, the data assimilation (DA) method was employed to integrate the vertical deformation obtained from the small baseline subset (SBAS) InSAR processing into the NASA catchment land surface model (CLSM), which improved the estimation of the TWS. First, we used a one-dimensional ensemble Kalman filter for DA research to estimate the TWS in Dali Prefecture, southwestern China. Finally, we compared the estimated TWS with the GRACE-based TWS from December 2, 2018 to January 21, 2021. The unbiased root-mean-square of the open loop (OL; without DA) method and the SBAS-InSAR DA method are 61 mm and 30 mm in Dali Prefecture, respectively. Results revealed that the numerical difference between the estimated TWS and the GRACE TWS retrievals was significantly decreased by the SBAS-InSAR DA method than the OL method. In addition, the temporal resolution of the SBAS-InSAR DA-based TWS was improved to 12 days compared with GRACE-based TWS. Furthermore, we recovered the discontinuous deletion and blank of GRACE-based TWS from 2015 to 2018 by the SBAS-InSAR DA method.

Index Terms—Catchment land surface model (CLSM), data assimilation (DA), ground deformation, small baseline subset (SBAS) InSAR, terrestrial water storage (TWS).

I. INTRODUCTION

THE uneven spatiotemporal distribution of terrestrial water resources is a serious problem troubling the survival and development of the human society. Moreover, the terrestrial water resource is an essential factor affecting the regional climate change and the ecological environment. Therefore, it is crucial to accurately estimate the terrestrial water storage (TWS) [1]. However, due to the limited coverage of the network space, it

is a challenge to obtain a large-scale TWS with high accuracy using conventional ground observations [2], [3]. Estimating the variations of TWS by land surface models (LSMs) is similarly hindered by LSM characteristics, model parameters, and meteorological conditions [4]. The gravity recovery and climate experiment satellite (GRACE) launched in March 2002 has unprecedented accuracy in capturing the medium and long wave parts of the Earth's gravity field [5]. The GRACE provides a new method for analyzing the seasonal and long-term changes of TWS [6]. However, the discontinuous GRACE data from 2011 to 2018 [7] has perplexed the research on terrestrial water reserves. Moreover, the low spatiotemporal resolution (∼400 km and ∼monthly [5]) in GRACE-based TWS monitoring data limits its application in small regions and submonthly scales.

Data assimilation (DA) is a conciliatory process between the measurement and the estimate with uncertain boundary. The DA uses specific rules (or algorithms) to process two kinds of data that are complementary in time or space. Thus, we can obtain more accurate and richer information than any single data [8]. Using DA to optimize TWS adds GRACE-based TWS to LSMs and effectively refine the spatial and temporal resolution of TWS [9]. The GRACE TWS anomalies (the change in TWS after deducting the long-term average) were first assimilated into the catchment land surface model (CLSM) by using the Kalman smoother (ENKS) filters in 2000 [10]. Compared with open loop (OL; without DA), the estimation of groundwater change assimilation has a higher correlation with the measured groundwater [9]. GRACE DA has been used in drought studies in North America [11] and Western and Central Europe [12]. The GRACE-DA-based TWS could be used to replace the lack of groundwater and soil moisture measurements [11], [12]. In recent years, many researchers have carried out a lot of complementary work on improving GRACE DA capacity [13]–[15] and multiple assimilations [16], [17].

In addition, using the DA to process the vertical deformation derived from the elastic response of the Earth's surface is another approach to estimate the TWS. The global positioning system (GPS) DA experiments demonstrated the ability of data fusion methods to estimate TWS variations using temporal vertical deformation [18]. Although using the vertical deformation observed by GPS to infer TWS changes can improve the temporal resolution, GPS observation stations are sparse and unevenly distributed in space. In addition, GPS data needs to be interpolated to obtain continuous spatial estimates of vertical deformations

The authors are with the Faculty of Geosciences and Environmental Engineering, Southwest Jiaotong University, Chengdu 610031, China (e-mail: kunchen2021@my.swjtu.edu.cn; rsgxliu@swjtu.edu.cn; xiangwei@my.swjtu.edu.cn; suntao@my.swjtu.edu.cn; qiankun@my.swjtu.edu.cn; caijiaxin@my.swjtu.edu.cn; sapirasteh@swjtu.edu.cn; xchen_rs@my.swjtu.edu.cn).
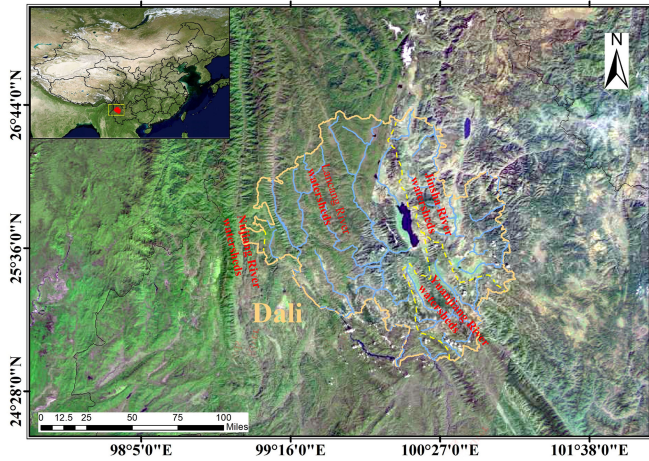
Fig. 1. River systems in the study area, the yellow dotted lines indicate the boundaries of different watersheds, the solid yellow line indicates the boundary of the study area.

TABLE I
ENSEMBLE PERTURBATION PARAMETERS FOR MODEL PROGNOSTIC VARIABLES IN THE NASA CATCHMENT LSM

	Unit	Type	Standard deviation	Temporal Correlation(day)
catdef	mm	A	0.15	1
SWE	mm	M	0.0012	1

SWE, snow water equivalent; A, additive perturbation; and M, multiplicative perturbation.

[19]–[21], which increases the uncertainty of using vertical deformation to infer TWS changes [22].

The small baseline subset (SBAS) InSAR technique developed in recent years provides a new alternative method for TWS estimation. Compared with the GPS method, the SBAS-InSAR method can obtain the surface deformation with high spatial resolution in a large scale [23]. It is a primary method for studying the movement mechanism of various geological activities. In the past few years, SBAS-InSAR has been widely used in the detection of surface deformation fields such as urban subsidence [24], volcanic deformation [25], surface deformations associated with earthquakes [26], and even the elastic response of the Earth's surface to the rainy season [27]. However, there are relatively few studies on using the SBAS-InSAR technique to estimate the TWS.

The purpose of this study was to demonstrate whether the time-series deformation obtained by the SBAS-InSAR and DA processing can estimate the TWS. The time-series deformation obtained by SBAS-InSAR was added to the DA framework to improve the inversion precision of the TWS for the first time. For validation purposes, we conducted a DA experiment in Dali Prefecture, which is a draught-prone area in the southwestern part of Yunnan Province. The TWS estimates were validated by using the GRACE inversion results.

II. MATERIALS AND METHODS

A. Study Area

Dali Prefecture is located at the junction of the Yunnan-Guizhou Plateau and Hengduan Mountains (Fig. 1). The elevation of the study area is higher in the northwest and lower in the southeast, with complex and diverse landforms. There are several large lake basins in the prefecture. There are 18 basins with an area of more than 1.5 km^2, covering a total area of 1871.49 km^2, accounting for 6.6% of the prefecture's total area. There are more than 160 rivers in the shape of plumes throughout

the region. The area includes four river systems: Jinsha River, Lancang River, Nujiang River, and Red River (Yuanjiang).

The study area has a typical subtropical karst landscape, sensitive to climate change, environmental change, and human activities. Jointly controlled by multiple monsoon systems, especially the Asian monsoon climate, Dali Prefecture is prone to drought, accompanied by severe soil erosion and ecological degradation [28]–[30]. The regional difference and abrupt changes in climate in this area are pronounced. According to the water resources bulletin (1962~2020) shared on Dali People's Government portal[1], the annual average temperature and precipitation are 15.8°C and 836 mm in the study area, respectively. And the annual rainfall is mainly concentrated in summer. Taking 2020 as an example, precipitation from June to August in Dali Prefecture accounts for 58.8% of the yearly rainfall.

B. Predictive Land Surface Model

NASA CLSM [10], [31] was used in this study, which is a terrestrial model component of the Goddard Earth Observing System. Compared with traditional soil-based LSMs, CLSM significantly simulates the horizontal heterogeneity of soil moisture and defines its impact on evapotranspiration and runoff [10]. In addition, CLSM also includes an essential representation of changes in shallow (unconfined) groundwater reserves [32]. However, CLSM cannot adequately simulate dynamic surface water hydrology or deeper multilayer aquifers [16]. Meanwhile, CLSM does not consider surface storage and anthropogenic water resource management [32], [33], which weakens its response to TWS changes in surface water storage.

The three CLSM prognostic variables are used to define the rootzone excess(rzexc), surface excess (srfexc), and catchment deficit (catdef). The catchment deficit is defined as the average increase in water depth required to make the catchment to saturation. The perturbation parameters for model prognostic variables are shown in Table I following Yin *et al.* [18].

CLSM was established on the Equal-Area Scalable Earth Grid 2.0 [34] at 625 km^2 ($=$ 25 km×25 km), with a 1-day interval. However, in this study, CLSM was used from December 2, 2018 to January 20, 2021, with an interval of 12 days. The study period and the time resolution were determined by the data availability of GRACE and the looking into continents from space with synthetic aperture radar (LiCSAR) [35]. The GRACE system provided data from April 2002 to February

[1][Online]. Available: http://www.dali.gov.cn/dlrmzf/c100639/common_list.shtml

TABLE II
LiCSAR FRAMES, OBSERVATION PERIODS, AND NUMBER OF DATA

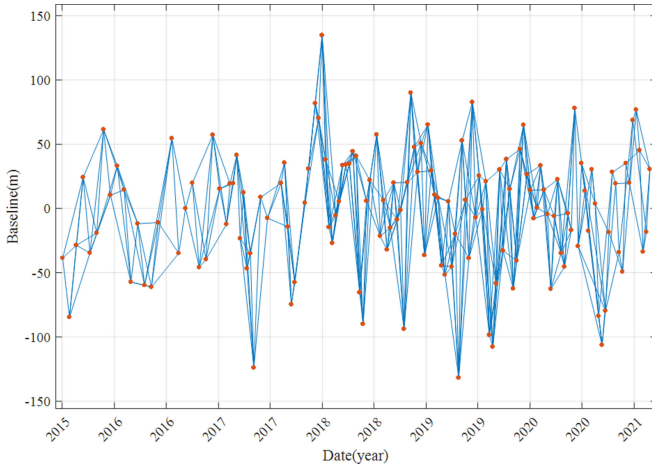| Frame ID | Date(yyyymmdd) | | Period (year) | # Image | # IFG | Average incidence angle (°) |
	Start	End				
099A_06414_131313	20141012	20210225	6.3	149	477	33.9615
135D_06418_131313	20141026	20170308	2.4	24	75	33.9806
	20180619	20210227	2.7	74	228	
033D_06301_131313	20160529	20170909	1.3	14	39	33.8370
	20181103	20191228	1.2	25	95	

IFG: interferograms.

Fig. 2. Spatiotemporal baselines of the interferograms derived from 155 images.

2021, but GRACE data from January 2011 to September 2018 were missing uninterrupted. Comet-liCSAR website provides LiCSAR data covering Dali Prefecture from November 5, 2014 to February 25, 2021, with a minimum interval of 12 days. This study used GRACE data after two months of the continuous regular operation of GRACE satellites; therefore, the study period was shortened to December 2, 2018, solstice, January 20, 2021.

C. SBAS-InSAR Measurement

The Sentinel-1 unwrapped, geocoded interferogram and the corresponding coherent data (0.001° resolution) were published on the Comet-LiCSAR website[2] after processing by the LiCSAR system [35]. As of May 1, 2021, there are 3 frames (1 and 2 in ascending and descending orbits, respectively) covering Dali (Table II). LiCSAR frame ID is NNND_AAAAA_BBBBBB, with NNN, D, AAAAA, and BBBBBB denoting the number of the relative orbit, the orbital direction, the colatitude identifier, and the number of included bursts, respectively [35]. In this study, the descending orbital data are not used, because the number of data is small (Table II). Among the 477 interferograms obtained from the ascending data, 448 interferograms from July 3, 2015 to February 25, 2021 were selected to monitor the temporal deformation. The spatiotemporal baselines of the interferograms are shown in Fig. 2. The average time interval
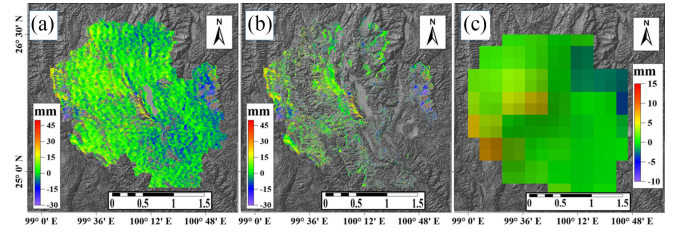
[2][Online]. Available: https://comet.nerc.ac.uk/COMET-LiCS-portal/

Fig. 3. LOS deformation in Dali Prefecture from July to September in 2020. (a) Deformation map before masking the pixes with large deformation rate. (b) Deformation map after the masking. (c) Deformation map after down-sampling.

for the ascending data before the end of 2016 was 24 days. After 2017, with the launch of Sentinel-1B, the time interval was reduced to 12 days [35]. When the study area is located within the area monitored by the Looking Inside the Continents from Space (LCS) project, its products can be obtained directly without downloading and preprocessing steps. The atmospheric phase in the interferogram was corrected by using the tropospheric delay product provided by Generic Atmospheric Correction Online Service (GACOS) system [36].

Before obtaining the time-series deformation of the surface and applying it to the TWS estimation, it is necessary to remove the subsidence funnel and the point of sharp uplift. To minimize the influence of deformation caused by non-TWS changes on DA, threshold method was adopted in this study to eliminate the points with absolute deformation rate greater than 5 mm. In addition, it is necessary to conduct down-sampling processing (by averaging the deformations of all pixes in each grid, and the averaged deformation is the grid value.) and convert line-of-sight (LOS) deformation measurement data into the vertical direction. The transformation function can be expressed as follows:

$$S_{vertical} = S_{los}/\cos\left(\beta\right) \tag{1}$$

where $S_{vertical}$ and S_{los} represent the vertical deformation, and the LOS deformation, respectively, and β represents average incidence angle.

As shown in Fig. 3, the surface temporal deformation of SBAS-InSAR was down-sampled to a 25 km×25 km grid. Fig. 3(a) shows the deformation map before masking the pixes with large deformation rate, Fig. 3(b) shows the deformation map after the masking, and Fig. 3(c) shows the deformation map after down-sampling. The vertical surface deformation from July to September in 2020 in Dali Prefecture is calculated using the down-sampled results. Each image in the SBAS-InSAR results will be down-sampled and transformed to vertical deformation. According to the water resources bulletin of Dali Prefecture, there is very little groundwater exploitation in Dali Prefecture, so we believe that the surface deformation is caused by the change of mass load. The changes of vertical deformation observation are affected by TWS changes and nonhydrological loads such as atmosphere and tide. This study considered that the influence of atmosphere and hydrology is negligible compared with that of hydrology. Therefore, this study directly uses the vertical surface deformation obtained by SBAS-InSAR without removing atmospheric and tidal effects for TWS estimation.
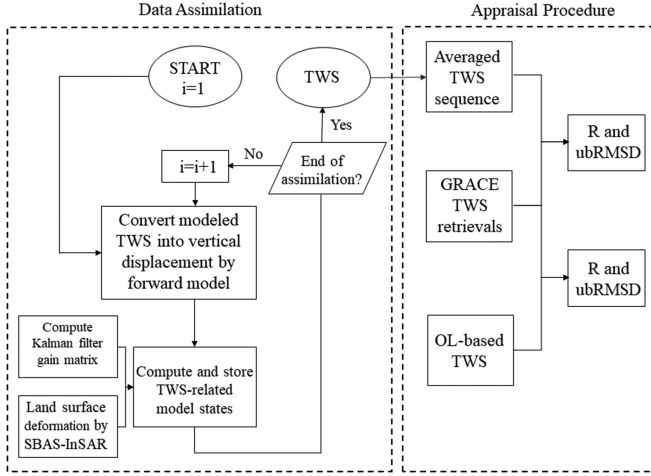
Fig. 4. Simplified flowchart of the SBAS-InSAR DA.

D. Framework of Data Assimilation

In this study, TWS via CLSM is used as the prior (unconditioned) estimate of Green's function forward model and EnKF. First, the modeled TWS was converted into the vertical deformation by Green's function forward model. Then, we computed and stored the TWS-related model states. Finally, we repeated the simulation for N times, and the optimal TWS estimation is obtained. The simplified flowchart of SBAS-InSAR DA is shown in Fig. 4.

1) Ensemble Kalman Filter: The one-dimensional (1-D) integrated Kalman filter [37] framework was adopted to assimilate the temporal surface deformation based on LiCSBAS into the LSM. An essential feature of 1-D EnKF is that the computational units are processed independently, with the minimum spatial error correlation between the different departments. The EnKF is flexible in the treatment of error in LSMs [38]. The EnKF has been triumphantly applied to soil moisture and snow inversion [39], [40]. However, EnKF is used to estimate the TWS by processing the time series deformation of the SBAS-InSAR for the first time. The model state and error covariance matrix based on the mean and spread of ensemble members are used in the Bayesian merging process of the LSM and SBAS-InSAR time-series deformation [18].

The EnKF carries out two steps in the execution process: prediction and measurement update. In the prediction process, the TWS state vector $x_t^{i-}(i = 1, \ldots, N)$ obtained from the LSM is taken as the prior estimate of the model at time t. The model forecast x_t^- is given by the ensemble mean. During the propagation phase, the updated state vector x_t^{i+} is calculated by the following equation:

$$x_t^{i+} = x_t^{i-} + K_t[y_t - H(x_t^{i-})] \tag{2}$$

where K_t is the Kalman filter gain matrix, y_t is the observation value at time t, and $H(.)$ is the Green's function forward model that transforms the model-like state vector into the surface deformation. K_t is used to assign the weight between the estimated and the observed values, and K_t is related to the observation

accuracy, which is calculated by the following equation:

$$K_t = Cov\left[x_t^-, H\left(x_t^-\right)\right] \left[Cov\left[H\left(x_t^-\right), H\left(x_t^-\right)\right] + C_{vv}\right]^{-1} \tag{3}$$

where $Cov[x_t^-, H(x_t^-)]$ expresses the error covariance of the prior TWS estimate of the model and the predicted observations, $Cov[H(x_t^-), H(x_t^-)]$ express the error covariance of the predicted observations, and Cvv expresses the observation error covariance.

In this study, $N = 24$ ensemble replicates were used following the GRACE TWS DA procedure outlined in Girotto *et al.* [16]. The standard deviation of observation error is 9 mm, including the errors (i.e., decoherence, DEM error, baseline error) during SBAS-InSAR data processing. See Section III.B for a further description of the standard deviation of observation error.

2) Green's Function Forward Model: According to previous studies [41], when surface water, ice and snow, and atmosphere act on the solid Earth, the Earth's surface will produce deformation. Deformation of the Earth by surface loads includes horizontal and vertical directions, and the vertical deformation is sensitive to the load source. In addition, the TWS variation can be mapped to the vertical surface deformation by using Green's function. Therefore, based on the Preliminary Production Earth Model (PREM) [42], this study used Green's function forward model [43] as the observation operator. Assuming that there is a water quality disk nuclear load with an angular radius α on the surface of the Earth. The Green's function of the vertical deformation S_{up}, caused by the water disk can be expressed as follows:

$$S_{up} = \sum_{n=0}^{\infty} h_n \Gamma_n \frac{4\pi Ga}{g(2n+1)} P_n(\cos\theta) \tag{4}$$

where P_n is the Legendre polynomial of degree n; θ is the angular distance from observation position to the center of the disk; G is the gravitational constant; a is the radius of the Earth; h_n is the load love number(LNN); and g is the gravitational acceleration. In this study, $h_1 = -0.284$ was used corresponding to the LNN for elastic Earth model PREM [44]. The derivation formula of the Γ_n function is as follows:

$$\Gamma_n = \frac{1}{2}\left[P_{n-1}(\cos\alpha) - P_{n+1}(\cos\alpha)\right] \tag{5}$$

$$\Gamma_0 = \frac{1}{2}(1-\cos\alpha). \tag{6}$$

In this study, CLSM was run on a 625 km^2 (= 25 km×25 km) EAE-Grid 2.0 [34]. The area of the grid is roughly equal to the disc with a radius of 14 km. Fig. 5 shows The ground deformation response to a homogeneous disc load with an equivalent water height of 1 m and a radius of 14 km. The most significant feature is that the vertical deformation maximizes in the center of the disc and then decreases rapidly away from the center. At the edge of the disk, the resulting vertical deformation is about 1.5 mm. The vertical deformation can be ignored when the distance from the center of the disk exceeds 300 km. The OL-based vertical deformation of each point on the land surface is calculated by convolving the impact of the TWS changes for each 25 km × 25 km pixel on the land surface [22].
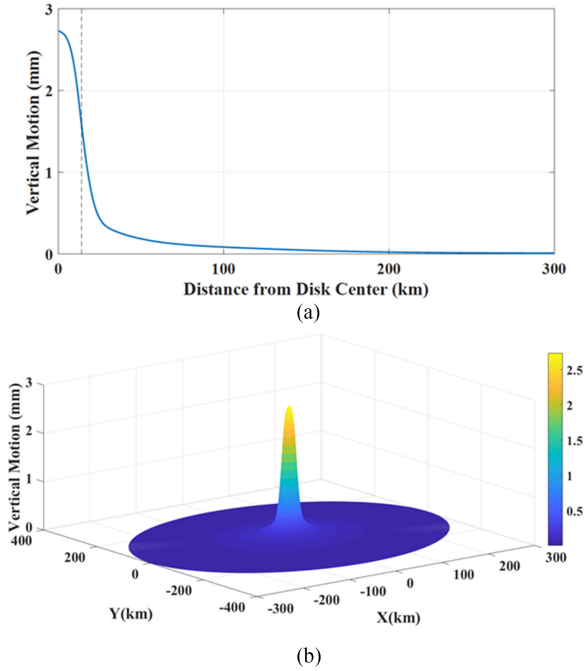
Fig. 5. Ground deformation response to a homogeneous disc load with an equivalent water height of 1 m and a radius of 14 km. (a) Schematic diagram of 1-D vertical deformation, where the dashed line represents the edges of the disk. (b) 3-D schematic diagram of vertical deformation.

It should be noted that the TWS changes outside the research area still influence the vertical deformation. The results may lead to some discrepancy between the SBAS-InSAR-based observations and the vertical deformation prediction observations based on Green's function. In order to reduce this discrepancy during DA simulation, the area used in the model to estimate the deformation should be larger than the TWS study area. In this way, the model-based predicted vertical deformation was effectively included in the vertical deformation caused by TWS variations outside the study area.

E. Appraisal Procedure

The TWS estimates from OL, and SBAS-InSAR DA simulations were evaluated with the TWS by the GRACE inversion. In this study, to quantify the accuracy of the model estimation, Unbiased root-mean-square difference (ubRMSD) and correlation coefficient (R) were used [18].

1) GRACE TWS: The validation data is the result of a 2-stage GRACE terrestrial grid(25 km×25 km) TWS inversion based on the Releasing 06 (RL06) spherical harmonic function provided by the Center for Space Research (CSR), University of Texas.[3] The TWS product of GRACE inversion is used to evaluate the accuracy of OL-based TWS and SBAS-InSAR DA-based TWS. Based on the inversion period of GRACE TWS [45], the OL-based TWS and SBAS-InSAR DA-based TWS were converted into monthly averages, and these results were then evaluated using GRACE TWS inversion.

[3][Online]. Available: http://www2.csr.utexas.edu/grace/RL06_mascons.html

2) Appraisal Indicators: Both the TWS from the inversions of OL and SBAS-InSAR DA were compared with TWS based on GRACE. R and ubRMSD were used to quantify the differences in the model estimate relative to the measured values. The consistency of time variations between model estimates and measurements can be reflected by R. It can be expressed as follows:

$$R = \frac{\sum\limits_{N_t}^{t=1} \left(x_{est,t} - \overline{x_{est}}\right)\left(x_{meas,t} - \overline{x_{meas}}\right)}{\sqrt{\sum\limits_{N_t}^{t=1} \left(x_{est,t} - \overline{x_{est}}\right)^2 \sum\limits_{N_t}^{t=1} \left(x_{meas,t} - \overline{x_{meas}}\right)^2}} \quad (7)$$

where N_t is the months' number during the study period; $x_{est,t}$ is an average population estimate calculated from OL-based TWS or DA-based TWS at time t; $x_{meas,t}$ is the measured value at time t; and $\overline{x_{est}}$ and $\overline{x_{meas}}$ represent the time-average variables obtained by model estimation and measurement, respectively.

The greater the amplitude and phase discrepancy between different data sets, the greater the ubRMSD. After subtracting the long-term average between the estimate and the measured value, the calculation of ubRMSD can be expressed as follows:

$$ubRMSD = \sqrt{\frac{1}{N_t}\sum\limits_{N_t}^{t=1}\left(x_{est,t} - x_{meas,t}\right)^2 - \left(\overline{x_{est}} - \overline{x_{meas}}\right)^2}. \quad (8)$$

III. RESULTS

A. Deformation in Dali Prefecture

In order to monitor the temporal and spatial variation trend of land subsidence in Dali Prefecture from 2015 to 2021, the LiCSBAS interferometric synthetic aperture radar method was used to detect the ground deformation. Fig. 6 shows the temporal deformation velocity of Dali Prefecture from 2015 to 2021. As can be seen from the figure, there is no large-scale surface subsidence or uplift in Dali Prefecture. The annual deformation rate is small on the whole, with the annual deformation rate ranging from −5 to 5 mm/year in most areas. In Fig. 6, three points (A, B, and C) were selected along the diagonal direction of the research area, and the time-series deformation diagram was shown in Fig. 7(a). It can be seen from the figure that the surface deformation at the selected site is stable all year-round, and there is apparent seasonal deformation in the year. In the region with noticeable seasonal variation, the maximum annual amplitude of surface deformation can reach 60 mm. In Fig. 6, there are two subsidence funnel areas with deformation rates significantly exceeding 5 mm/year in the eastern part of Dali, which cannot be caused by TWS changes. Therefore, points with the same time series trend with points D and E will be deleted, before the SBAS-InSAR DA. In Binchuan County (D), as shown in Fig. 7(b), the maximum subsidence from 2015 to 2021 is greater than 100 mm; In Xiangyun County (E), as shown in Fig. 7(b), the maximum subsidence from 2015 to 2021 is greater than 140 mm.
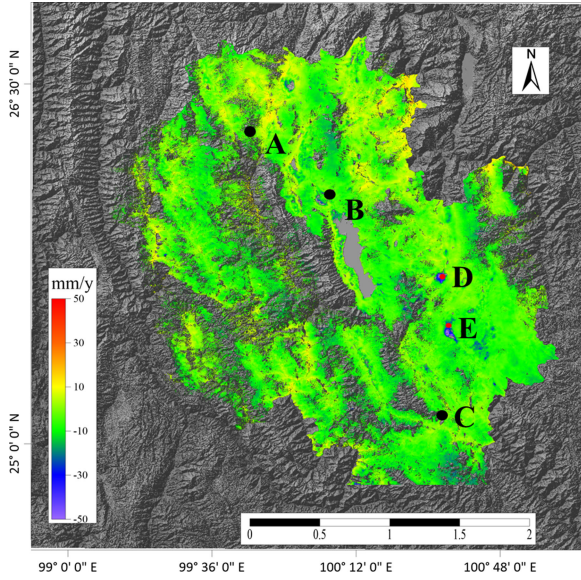
Fig. 6. Temporal deformation velocity of Dali Prefecture from 2015 to 2021. The feature points A, B, and C are selected for the seasonal subsidence analysis, D and E are selected for the subsidence funnels analysis.
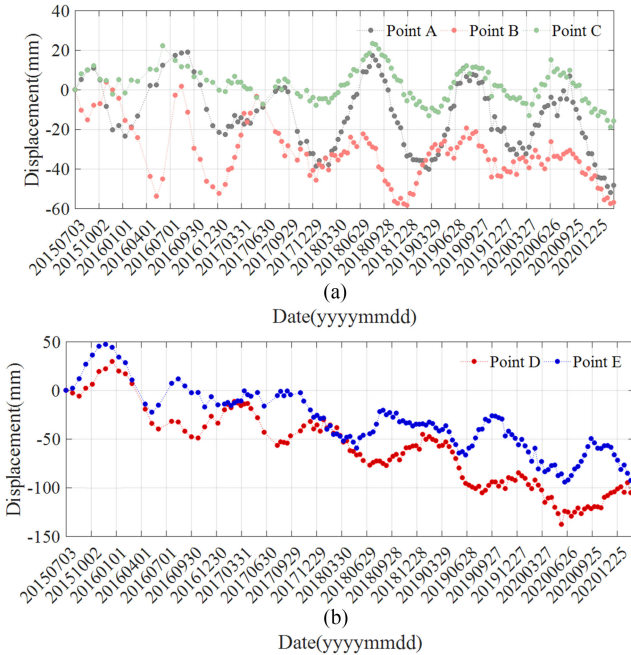

(a)

(b)

Fig. 7. Time-series deformation of the selected feature points. (a) Time-series deformation of the selected points (A, B, and C) along the diagonal of the study area. (b) Time-series deformation of the two obvious subsidence funnels.

B. Normalized Innovation Sequence

In this study, we intend to use normalized innovation (NI) series to test the suitability of the specified error standard deviation in the DA processing [33]. It is assumed that all errors are independent of each other and conform to the Gaussian distribution and both the CLSM and the observation operator are linear. If the DA is optimal in the sense of minimum variance,
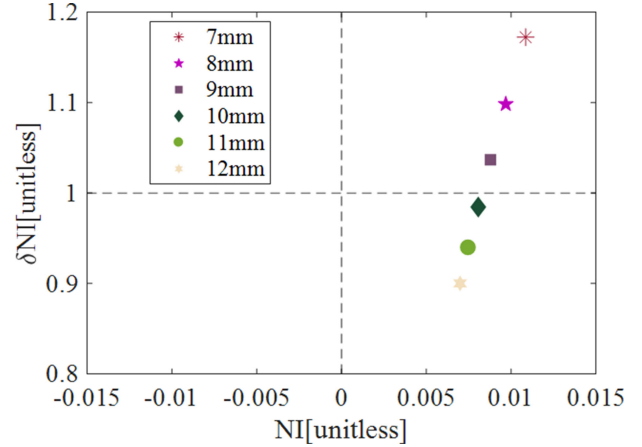

Fig. 8. Dali Prefecture SBAS-InSAR DA NI sequence statistics. Different markers represent the different standard deviations of observation errors (7 to 12 mm).

then the NI sequence should meet a Gaussian distribution with a standard deviation of 1 and mean 0 [46]. In this study, given that these assumptions are not fully fulfilled, we need to explore the NI sequence to provide helpful support into the SBAS-InSAR DA method. The following formula can express the relationship between the NI sequence and time in the study region by using the average estimation of time t:

$$NI_t = \frac{y_t - H\left(x_t^-\right)}{\sqrt{C_{vv} + Cov\left[H\left(x_t^-\right), H\left(x_t^-\right)\right]}}. \quad (9)$$

The numerator represents the difference between the measured value and the simulated value calculated by the forward model. The denominator represents the square root of the sum of the observation error covariance and the observation prediction error covariance. Then, the time mean $(\overline{NI})$ and time standard deviation (σ_{NI}) of NI were calculated using the study area mean NI sequence. Finally, the different values of the standard deviation of observation error (from 7 to 12 mm) in the SBAS-InSAR DA simulation process were tested, the corresponding $\overline{NI}$ and σ_{NI} of Dali Prefecture are calculated, as shown in Fig. 8.

It can be seen from Fig. 8 that the values calculated by using the standard deviations of different observation errors $\overline{NI}$ are all greater than 0. This suggests that the model predictions contain a seasonal bias relative to the SBAS-InSAR observations where the model contains too little water during certain times of the year. This can be seen via Fig. 9, where the SBAS-InSAR DA effectively increases equivalent water height at foot. With the measurement error standard deviation increasing, the time standard deviation σ_{NI} tends to decrease, and $\overline{NI}$ tends to approach 0. In other words, in the process of DA, due to noise in the SBAS-InSAR measured value, the weight of the SBAS-InSAR measured value will be reduced to obtain a more accurate estimate value. For example, according to Fig. 8, when the standard deviation is 9 or 10 mm, the measured data can occupy an appropriate weight in the assimilation process and obtain more accurate DA results.
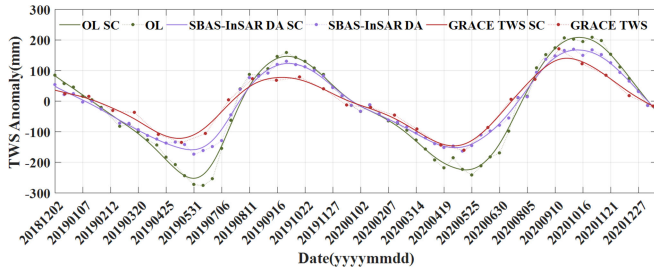
Fig. 9.   Average TWS anomalies time series from December 2018 to January 2021. The green line indicates the OL SC (Spline Curve), the purple line indicates the SBAS-InSAR SC, and the red line indicates the GRACE TWS SC.
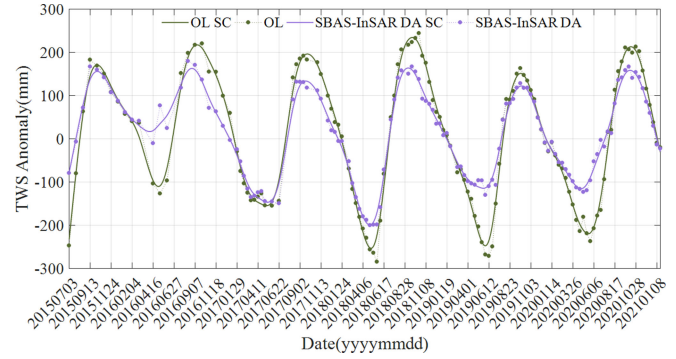

Fig. 10.   Average TWS anomalies time series from July 2015 to January 2021. The green line indicates the OL SC (Spline Curve) and the purple line indicates the SBAS-InSAR SC.

TABLE III
STUDY AREA CORRELATION COEFFICIENT (R) AND UNBIASED
ROOT-MEAN-SQUARE DIFFERENCE (ubRMSD) COMPUTED BETWEEN GRACE
TWS RETRIEVALS AND THE ENSEMBLE MEAN OF ESTIMATED TWS
ANOMALIES (I.E., THE OL AND SBAS-InSAR DA)

	OL		SBAS-InSAR DA	
Periods	R	ubRMSD(mm)	R	ubRMSD(mm)
201812-201912	0.963	65	0.960	33
201912-202101	0.969	56	0.976	25

C. Terrestrial Water Storage Changes of Dali Prefecture

The average TWS anomalies time series simulated by OL and SBAS-InSAR DA and the independent GRACE TWS retrievals results are shown in Fig. 9. For seasonal variations of TWS, three different datasets all show good consistency. The amplitude of the TWS based on the SBAS-InSAR DA is generally smaller than that of OL, with a tendency to add water mass from May to June and reduce mass from September to October. The amplitude range of TWS obtained by the SBAS-InSAR DA method is smaller than that obtained by CLSM directly, thus reducing the uncertainty of TWS estimation using the DA method.

Daily estimates of OL and SBAS-InSAR DA for the entire TWS study period (December 2018 to January 2021) were converted to monthly averages based on the GRACE TWS retrievals period. First, the correlation coefficients R and ubRMSD between the average TWS values (i.e., OL and SBAS-InSAR DA) obtained by the model and GRACE TWS retrievals were calculated. Then the mean R and ubRMSD of Dali Prefecture for different study periods are calculated, as shown in Table III. The R of SBAS-InSAR DA was slightly smaller throughout the study period than the OL (0.960 and 0.964 for SBAS-InSAR and OL, respectively). However, there was a significant difference in ubRMSD (30 mm for SBAS-InSAR and 61 mm for OL).

In this study, the surface vertical deformation time series obtained by SBAS-InSAR and CLSM was used to calculate the TWS changes of Dali Prefecture from 2015 to 2021 according to the DA framework. As can be seen from Fig. 10, the SBAS-InSAR DA TWS in May 2016 was significantly higher than that in adjacent months (this result may be problematic and will be further analyzed in the discussion section of this article). In addition, the TWS changes in Dali Prefecture have distinct seasonality, with its maximum value in October (late summer) and its minimum value in April (late winter). The maximum annual amplitude of TWS in Dali obtained by SBAS-InSAR DA from 2017 to 2021 is about 360 mm; the minimum value is about 220 mm.

IV. DISCUSSION

A. Anomaly of Average Terrestrial Water Storage

The vertical deformation of the Earth's surface is affected by geological activities such as volcanic eruptions and earthquakes, which all affect the accuracy of TWS estimation. In Fig. 10, the most obvious feature is the abnormal increase of SBAS-InSAR DA TWS from May to June 2016, which may be due to the abnormal surface deformation caused by the M5 earthquake[4] in Yunlong County, Dali Prefecture on May 18, 2016. DA adds this information to the TWS estimate, resulting in an abnormal increase in the TWS. Therefore, this part of the data cannot be considered a reliable estimate of TWS. Thus, the data of May and June should be removed from the TWS data recovered in this study.

B. Spatial Distribution Characteristics of R and ubRMSD

R and ubRMSD of a single-pixel in the study area were computed between the modeled TWS anomalies (i.e., the OL and SBAS-InSAR DA) and GRACE TWS retrievals during the study period.

The spatial distribution of R and ubRMSD is shown in Fig. 11. Fig. 11(a) and (b), respectively, show the R derived by the GRACE TWS retrievals and the estimated TWS anomalies (i.e., the SBAS-InSAR DA and OL), respectively. As can be seen, R was high for both methods throughout the study period. However, the R between SBAS-InSAR DA TWS and GRACE retrievals in some pixels is lower than that between OL TWS and GRACE retrievals. This may be because the surface deformation data obtained from the downsampling cannot accurately represent the deformation caused by TWS changes. It can be seen from the figure that the most significant feature is that the ubRMSD of SBAS-InSAR DA is lower than that of OL in the whole study area. The reduction of ubRMSD indicates that the
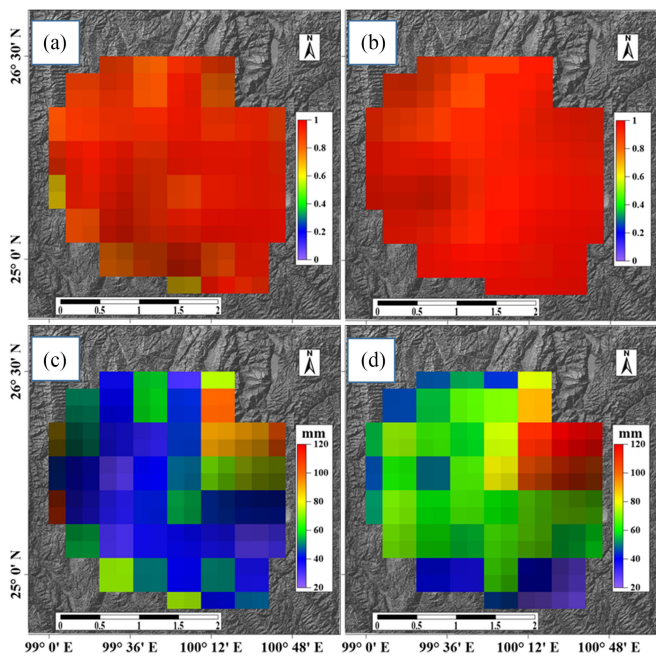
[4][Online].   Available: http://www.yndzj.gov.cn/yndzj/300518/371724/371726/index.html

Fig. 11. Spatial distribution of the correlation coefficient (R) and the unbiased root-mean-square difference (ubRMSD). (a) and (b) R derived by the GRACE TWS retrievals and the estimated TWS anomalies (i.e., the SBAS-InSAR DA and OL), respectively. (c) and (d) ubRMSD derived by the GRACE TWS retrievals and the estimated TWS anomalies (i.e., the SBAS-InSAR DA and OL), respectively.

method of SBAS-InSAR has a better performance in reducing the difference with GRACE TWS. It should be noted that in the northeastern part of Dali Prefecture (Jinsha River Basin), both SBAS-InSAR and OL methos showed large ubRMSD. Especially, the OL method has a maximum ubRMSD of 120 mm during the study period. This large ubRMSD may be because the changes of surface water reserves (such as lakes and rivers) are not fully reflected in the CLSM [13].

V. CONCLUSION

Surface temporal series deformation obtained by SBAS-InSAR provides vertical deformation indirectly related to TWS. This study is the first time to assimilate the SBAS-InSAR time-series vertical deformation into the LSM based on the Earth elastic load theory (the elastic response of solid Earth to load changes). To acquire more reliable TWS estimation, the SBAS-InSAR time-series vertical deformation is integrated into the LSM through the DA processing.

The TWS obtained from SBAS-InSAR DA and OL were evaluated using GRACE TWS. For the whole study area, the average TWS changes obtained by SBAS-InSAR DA and OL demonstrate the superiority of the SBAS-InSAR DA method. In particular, the SBAS-InSAR DA improved ubRMSD and reduced the average TWS ubRMSD in Dali Prefecture from 61 to 30 mm. However, for R and ubRMSD of a single pixel, there are some unsatisfactory results. In some pixels, the value of R is lower after DA than before. The ubRMSD values of the two methods are both too high in some areas, which may be caused by the CLSM's lack of the explicit river regulation modeling.

More work toward obtaining the permanent scatterer points containing rich information of TWS changes of TWS estimates is needed in the future. Additionally, to provide more valuable guidance for the DA processing, the influence of the down-sampling method on the vertical deformation of the grid and the SBAS-InSAR DA results need to be further explored. Despite these potential problems, the findings of this study suggest that the SBAS-InSAR DA method can be used to recover GRACE data missing and provide an informative reference for other studies.

REFERENCES

[1] V. Ferreira *et al.*, "Prospects for imaging terrestrial water storage in south America using daily GPS observations," *Remote Sens.*, vol. 11, no. 6, 2019, Art. no. 679.

[2] C. C. Chew and E. E. Small, "Terrestrial water storage response to the 2012 drought estimated from GPS vertical position anomalies," *Geophysical Res. Lett.*, vol. 41, no. 17, pp. 6145–6151, 2014.

[3] T. H. Syed, J. S. Famiglietti, M. Rodell, J. Chen, and C. R. Wilson, "Analysis of terrestrial water storage changes from GRACE and GLDAS," *Water Resour. Res.*, vol. 44, no. 2, 2008, Art. no. W02433.

[4] E. F. Wood *et al.*, "Hyperresolution global land surface modeling: Meeting a grand challenge for monitoring Earth's terrestrial water," *Water Resour. Res.*, vol. 47, no. 5, 2011, Art. no. W05301.

[5] B. D. Tapley, S. Bettadpur, M. Watkins, and C. Reigber, "The gravity recovery and climate experiment: Mission overview and early results," *Geophysical Res. Lett.*, vol. 31, no. 9, 2004, Art. no. L09607.

[6] M. Zhong, J. Duan, H. Xu, P. Peng, H. Yan, and Y. Zhu, "Trend of China land water storage redistribution at medi- and large-spatial scales in recent five years by satellite gravity observations," *Sci. Bull.*, vol. 54, no. 5, pp. 816–821, 2008.

[7] J. S. Famiglietti and M. Rodell, "Environmental science. Water in the balance," *Science*, vol. 340, no. 6138, pp. 1300–1301, Jun. 2013.

[8] G. Evensen, "The ensemble Kalman filter for combined state and parameter estimation," *IEEE Control Syst. Mag.*, vol. 29, no. 3, pp. 83–104, Jun. 2009.

[9] B. F. Zaitchik, M. Rodell, and R. H. Reichle, "Assimilation of GRACE terrestrial water storage data into a land surface model: Results for the Mississippi River basin," *J. Hydrometeorol.*, vol. 9, no. 3, pp. 535–548, 2008.

[10] R. D. Koster, M. J. Suarez, A. Ducharne, M. Stieglitz, and P. Kumar, "A catchment-based approach to modeling land surface processes in a general circulation model: 1 Model structure," *J. Geophysical Res., Atmos.*, vol. 105, no. D20, pp. 24809–24822, 2000.

[11] R. Houborg, M. Rodell, B. Li, R. Reichle, and B. F. Zaitchik, "Drought indicators based on model-assimilated gravity recovery and climate experiment (GRACE) terrestrial water storage observations," *Water Resour. Res.*, vol. 48, no. 7, 2012, Art. no. W07525.

[12] B. Li, M. Rodell, B. F. Zaitchik, R. H. Reichle, R. D. Koster, and T. M. van Dam, "Assimilation of GRACE terrestrial water storage into a land surface model: Evaluation and potential value for drought monitoring in western and central Europe," *J. Hydrol.*, vol. 446-447, pp. 103–115, 2012.

[13] M. Girotto, G. J. M. De Lannoy, R. H. Reichle, and M. Rodell, "Assimilation of gridded terrestrial water storage observations from GRACE into a land surface model," *Water Resour. Res.*, vol. 52, no. 5, pp. 4164–4183, 2016.

[14] A. Eicker, M. Schumacher, J. Kusche, P. Döll, and H. M. Schmied, "Calibration/data assimilation approach for integrating GRACE data into the WaterGAP global hydrology model (WGHM) using an ensemble Kalman filter: First results," *Surv. Geophys.*, vol. 35, no. 6, pp. 1285–1309, 2014.

[15] M. Ek *et al.*, "Assimilation of gridded GRACE terrestrial water storage estimates in the North American land data assimilation system," *J. Hydrometeorol.*, vol. 17, no. 7, pp. 1951–1972, 2016.

[16] M. Girotto, R. H. Reichle, M. Rodell, Q. Liu, S. Mahanama, and G. J. M. De Lannoy, "Multi-sensor assimilation of SMOS brightness temperature and GRACE terrestrial water storage observations for soil moisture and shallow groundwater estimation," *Remote Sens. Environ.*, vol. 227, pp. 12–27, 2019.

[17] N. Tangdamrongsub *et al.*, "Multivariate data assimilation of GRACE, SMOS, SMAP measurements for improved regional soil moisture and groundwater storage estimates," *Adv. Water Resour.*, vol. 135, 2020, Art. no. 103477.

[18] G. Yin, B. A. Forman, and J. Wang, "Assimilation of ground-based GPS observations of vertical deformation into a land surface model to improve terrestrial water storage estimates," *Water Resour. Res.*, vol. 57, no. 2, 2021, Art. no. e2020WR028763.

[19] K. Chanard, J. P. Avouac, G. Ramillien, and J. Genrich, "Modeling deformation induced by seasonal variations of continental water in the Himalaya Region: Sensitivity to Earth elastic structure," *J. Geophysical Res., Solid Earth*, vol. 119, no. 6, pp. 5097–5113, 2014.

[20] Y. Fu and J. T. Freymueller, "Seasonal and long-term vertical deformation in the Nepal Himalaya constrained by GPS and GRACE measurements," *J. Geophysical Res., Solid Earth*, vol. 117, no. B3, 2012, Art. no. B03407.

[21] E. Knappe, R. Bendick, H. R. Martens, D. F. Argus, and W. P. Gardner, "Downscaling vertical GPS observations to derive watershed-scale hydrologic loading in the Northern Rockies," *Water Resour. Res.*, vol. 55, no. 1, pp. 391–401, 2019.

[22] G. Yin, B. A. Forman, B. D. Loomis, and S. B. Luthcke, "Comparison of vertical surface deformation estimates derived from space-based gravimetry, ground-based GPS, and model-based hydrologic loading over snow-dominated watersheds in the United States," *J. Geophysical Res., Solid Earth*, vol. 125, no. 8, 2020, Art. no. e2020JB019432.

[23] P. Berardino, G. Fornaro, R. Lanari, and E. Sansosti, "A new algorithm for surface deformation monitoring based on small baseline differential SAR interferograms," *IEEE Trans. Geosci. Remote Sens.*, vol. 40, no. 11, pp. 2375–2383, Nov. 2002.

[24] L. Zhou *et al.*, "Wuhan surface subsidence analysis in 2015–2016 based on Sentinel-1A data by SBAS-InSAR," *Remote Sens.*, vol. 9, no. 10, 2017, Art. no. 982.

[25] P. Tizzani *et al.*, "Surface deformation of Long Valley Caldera and Mono Basin, California, investigated with the SBAS-InSAR approach," *Remote Sens. Environ.*, vol. 108, no. 3, pp. 277–289, 2007.

[26] R. Lanari *et al.*, "Surface displacements associated with the L'Aquila 2009 mw 6.3 earthquake (central Italy): New evidence from SBAS-DInSAR time series analysis," *Geophysical Res. Lett.*, vol. 37, no. 20, 2010, Art. no. L20309.

[27] A. Rateb and E. Hermas, "The 2018 long rainy season in Kenya: Hydrological changes and correlated land subsidence," *Remote Sens.*, vol. 12, no. 9, 2020, Art. no. 1390.

[28] P. Lai *et al.*, "Responses of seasonal indicators to extreme droughts in Southwest China," *Remote Sens.*, vol. 12, no. 5, 2020, Art. no. 818.

[29] E. Lu *et al.*, "The day-to-day monitoring of the 2011 severe drought in China," *Climate Dyn.*, vol. 43, no. 1/2, pp. 1–9, 2013.

[30] E. Lu *et al.*, "The nonlinear relationship between summer precipitation in China and the sea surface temperature in preceding seasons: A statistical demonstration," *J. Geophysical Res., Atmos.*, vol. 120, no. 23, pp. 12 027–12 036, 2015.

[31] A. Ducharne, R. D. Koster, M. J. Suarez, M. Stieglitz, and P. Kumar, "A catchment-based approach to modeling land surface processes in a general circulation model: 2 Parameter estimation and model demonstration," *J. Geophysical Res., Atmos.*, vol. 105, no. D20, pp. 24823–24838, 2000.

[32] M. Girotto *et al.*, "Benefits and pitfalls of GRACE data assimilation: A case study of terrestrial water storage depletion in India," *Geophysical Res Lett*, vol. 44, no. 9, pp. 4107–4115, May 2017.

[33] B. A. Forman, R. H. Reichle, and M. Rodell, "Assimilation of terrestrial water storage from GRACE in a snow-dominated basin," *Water Resour. Res.*, vol. 48, no. 1, 2012, Art. no. W01507.

[34] M. J. Brodzik, B. Billingsley, T. Haran, B. Raup, and M. H. Savoie, "EASE-grid 2.0: Incremental but significant improvements for Earth-gridded data sets," *ISPRS Int. J. Geo-Inf.*, vol. 1, no. 1, pp. 32–45, 2012.

[35] M. Lazecký *et al.*, "LiCSAR: An automatic InSAR tool for measuring and monitoring tectonic and volcanic activity," *Remote Sens.*, vol. 12, no. 15, 2020, Art. no. 424.

[36] C. Yu, Z. Li, N. T. Penna, and P. Crippa, "Generic atmospheric correction model for interferometric synthetic aperture radar observations," *J. Geophysical Res., Solid Earth*, vol. 123, no. 10, pp. 9202–9222, 2018.

[37] R. H. Reichle, J. P. Walker, R. D. Koster, and P. R. Houser, "Extended versus ensemble Kalman filtering for land data assimilation," *J. Hydrometeorol.*, vol. 3, no. 6, 2002, Art. no. 728.

[38] G. J. M. De Lannoy, R. H. Reichle, P. R. Houser, K. R. Arsenault, N. E. C. Verhoest, and V. R. N. Pauwels, "Satellite-scale snow water equivalent assimilation into a high-resolution land surface model," *J. Hydrometeorol.*, vol. 11, no. 2, pp. 352–369, 2010.

[39] R. H. Reichle, "Global assimilation of satellite surface soil moisture retrievals into the NASA catchment land surface model," *Geophysical Res. Lett.*, vol. 32, no. 2, 2005, Art. no. L02404.

[40] Y. Xue, B. A. Forman, and R. H. Reichle, "Estimating snow mass in North America through assimilation of AMSR-E brightness temperature observations using the catchment land surface model and support vector machines," *Water Resour Res.*, vol. 54, no. 9, pp. 6488–6509, Sep. 2018.

[41] J. Wahr *et al.*, "The use of GPS horizontals for loading studies, with applications to Northern California and Southeast Greenland," *J. Geophysical Res., Solid Earth*, vol. 118, no. 4, pp. 1795–1806, 2013.

[42] A. M. Dziewonski and D. L. Anderson, "Preliminary reference Earth model," *Phys. Earth Planet. Interiors*, vol. 25, no. 4, pp. 297–356, 1981.

[43] W. E. Farrell, "Deformation of the Earth by surface loads," *Rev. Geophys.*, vol. 10, pp. 761–797, 1972.

[44] H. Wang *et al.*, "Load love numbers and Green's functions for elastic Earth models PREM, iasp91, ak135, and modified models with refined crustal structure from crust 2.0," *Comput. Geosci.*, vol. 49, pp. 190–199, 2012.

[45] C. Dahle *et al.*, "The GFZ GRACE RL06 monthly gravity field time series: Processing details and quality assessment," *Remote Sens.*, vol. 11, no. 18, 2019, Art. no. 2116.

[46] R. Mehra, "On the identification of variances and adaptive Kalman filtering," *IEEE Trans. Autom. Control*, vol. 15, no. 2, pp. 175–184, Apr. 1970.

Kun Chen received the B.Eng. degree in surveying engineering from Chang'an University, Xian, China, in 2019. Since 2019, he has been working toward the M.S. degree in photogrammetry and remote sensing with the Faculty of Geosciences and Environmental Engineering, Southwest Jiaotong University, Chengdu, China.
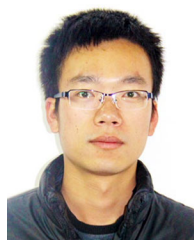
His current research interests include geological hazard monitoring and time series synthetic aperture radar applications.

Guoxiang Liu received the B.Eng. degree in surveying engineering from the East China Institute of Geology, Jiangxi, China, in 1991, the M.Eng. degree in geomatics from Southwest Jiaotong University, Chengdu, China, in 1994, and the Ph.D. degree in remote sensing from The Hong Kong Polytechnic University, Hong Kong, in 2003.

He is currently a Professor with the Department of Remote Sensing and Geospatial Information Engineering, Southwest Jiaotong University. From September 2005 to September 2006, he was a Visiting Scholar and conducted research on InSAR with Dr. S. M. Buckley with the Department of Aerospace Engineering and Engineering Mechanics, The University of Texas at Austin, TX, USA. He is the author of three books, more than 170 articles, and holds 12 patents. His current research interests include InSAR, PSI, radargrammetry and digital photogrammetry for mapping regional topography, and deformation.

Prof. Liu was a Co-Chair of the Working Group VII of the ISPRS Technical Commission VII, and a member of the Commission on Mapping from Satellite Imagery of the International Cartographic Association.

Wei Xiang received the B.Eng. and M.Eng. degrees in surveying engineering from the China University of Geosciences, Wuhan, China, in 2012 and 2014, respectively. Since 2017, he has been working toward the Ph.D. degree in photogrammetry and remote sensing with the Faculty of Geosciences and Environmental Engineering, Southwest Jiaotong University, Chengdu, China.

His current research interests include geological hazards monitoring, and time-series InSAR.

Tao Sun received the B.Eng. degree in surveying engineering from Changchun Institute of Technology, Changchun, China, in 2018. Since 2019, he has been working toward the M.S. degree in photogrammetry and remote sensing with the Faculty of Geosciences and Environmental Engineering, Southwest Jiaotong University, Chengdu, China.

His current research interests include deformation monitoring of super large bridges and time series synthetic aperture radar applications.

Kun Qian received the B.Eng. degree in surveying engineering from Southwest Jiaotong University, Chengdu, China, in 2019. Since 2019, he has been working toward the M.S. degree in photogrammetry and remote sensing with the Faculty of Geosciences and Environmental Engineering, Southwest Jiaotong University, Chengdu, China.

His current research interests include railway deformation monitoring and time series synthetic aperture radar.

Jiaxin Cai received the B.Eng. degree in surveying engineering from Southwest Petroleum University, Chengdu, China, in 2019. Since 2019, she has been working toward the M.S. degree in photogrammetry and remote sensing with the Faculty of Geosciences and Environmental Engineering, Southwest Jiaotong University, Chengdu, China.

Her current research interests include the cataloging and movement mechanism of stone glacier and time series synthetic aperture radar.

Saied Pirasteh received the Ph.D. degree in geology (remote sensing and GIS) from Aligarh Muslim University, Aligarh, India, in 2004, and the Ph.D. degree in geography (GIS, geoanalytics, and LiDAR) from the University of Waterloo, Waterloo, ON, Canada, in 2018.

He is currently an Associate Professor with the Faculty of Geosciences and Environmental Engineering, Southwest Jiaotong University, Chengdu, China. His research interests include remote sensing and LiDAR data processing and geology applications, environmental hazards, and disaster assessment toward implementing UN sustainable development goals 2030.

Dr. Pirasteh is the UN-GGIM Academic Network Member. He is also interested in integrating artificial intelligence, machine learning, computer vision, development of geospatial algorithms, models, software, mobile, and web app in geosciences applications.

Xiao Chen received the B.Eng. degree from Tianjin Chengjian University, Tianjin, China, in 2016 and the M.Eng. degree from Southwest Jiaotong University, Chengdu, China, 2019, both in surveying engineering. Since 2019, he has been working toward the Ph.D. degree in photogrammetry and remote sensing with the Faculty of Geosciences and Environmental Engineering, Southwest Jiaotong University, Chengdu, China.

His current research interests in algorithm research and application of Lidar.